Research Article | Vol. 31, No. 14 / 3 Jul 2023 / Optics Express 22964
Optics EXPRESS

Revised spectral optimization approach to remove surface-reflected radiance for the estimation of remote-sensing reflectance from the above-water method

JUNFANG LIN,[1,*] ZHONGPING LEE,[2] GAVIN H. TILSTONE,[1] XIAOHAN LIU,[1] JIANWEI WEI,[3,4] MICHAEL ONDRUSEK,[3] AND STEVE GROOM[1]

[1]Plymouth Marine Laboratory, Prospect Place, The Hoe, Plymouth PL1 3DH, UK
[2]State Key Laboratory of Marine Environmental Science, College of Ocean and Earth Sciences, Xiamen University, Xiamen 361102, China
[3]NOAA/NESDIS Center for Satellite Applications and Research (STAR), College Park, Maryland, USA
[4]Global Science & Technology, Inc., Greenbelt, Maryland, USA
*Junl@pml.ac.uk

Abstract: The effective sea-surface skylight reflectance (ρ) is an important parameter for removing the contribution of surface-reflected radiance when measuring water-leaving radiance (L_w) using the above-water approach (AWA). Radiative simulations and field measurements show that ρ varies spectrally. To improve the determination of L_w (and then remote sensing reflectance, R_{rs}) from the AWA, we further developed a wavelength-dependent model for ρ to remove surface-reflected radiance, which is applied with a spectral optimization approach for the determination of R_{rs}. Excellent agreement was achieved between the AWA-derived and skylight-blocked approach (SBA)-obtained R_{rs} (coefficient of determination > 0.92, mean absolute percentage deviation < ~ 11% for $R_{rs} > 0.0005$ sr^{-1}), even during high wave conditions. We found that the optimization approach with the new ρ model worked very well for a wide range of water types and observation geometries. For developing remote sensing algorithms and evaluating satellite products, it would be beneficial to apply this approach to current and historical above-water in situ measurements of R_{rs} to improve the quality of these data. In addition, this approach could also increase the number of useable spectra where previously rendered unusable when processed with a traditional scheme.

1. Introduction

Remote sensing reflectance (R_{rs}, sr^{-1}) is a fundamental physical quantity from satellite ocean color measurements. It is defined as the ratio of the water-leaving radiance (L_w, W/m^2/nm/sr) to the downwelling irradiance just above the sea surface (E_s, W/m^2/nm). Over the past four decades, several methods have been developed to measure R_{rs} in the field, which include in-water, on-water, and above-water methods [1–5]. Among these, the above-water approach (AWA) has become more popular, as measurement procedures and requirements for equipment by this scheme can be easily met. AWA data from platforms such as AERONET-OC are widely used for satellite ocean color validation [6].

The AWA platforms measure the total upwelling radiance (L_t, W/m^2/nm/sr) instead of directly measuring L_w. The radiance L_t that enters the detector can be accurately determined by the following equation, which takes into account both the sky radiance (L_s, W/m^2/nm/sr) incident onto the sea surface and the upwelling underwater radiance (L_u, W/m^2/nm/sr) onto the sea surface

#486981 https://doi.org/10.1364/OE.486981
Journal © 2023 Received 3 Feb 2023; revised 13 May 2023; accepted 5 Jun 2023; published 26 Jun 2023

Optics EXPRESS

from below [7]:

$$L_t(\lambda,\theta,\varphi\in\Omega_{FOV}) = \frac{1}{\Omega_{FOV}}\int_{\Omega_{FOV}}\left[\int_{2\pi_d} L_s(\lambda,\theta',\varphi')\cdot r(\lambda,\theta',\varphi'\rightarrow\theta,\varphi)d\Omega(\theta',\varphi')\right]d\Omega(\theta,\varphi) + \frac{1}{\Omega_{FOV}}\int_{\Omega_{FOV}}\left[\int_{2\pi_u} L_u(\lambda,\theta',\varphi')\cdot t(\lambda,\theta',\varphi'\rightarrow\theta,\varphi)d\Omega(\theta',\varphi')\right]d\Omega(\theta,\varphi) \tag{1}$$

where Ω_{FOV} is the solid angle of the detector field-of-view (FOV); θ and φ are zenith and azimuth angles of detector viewing geometry relative to the position of the sun, and (40°, 135°) are commonly recommended for optimal observations [7], thus $L_t(\lambda,\theta,\varphi\in\Omega_{FOV})$ denotes the average radiance at wavelength λ over the detector FOV when the detector is pointed in the nominal (θ,φ) direction. The radiance reflectance $r(\lambda,\theta',\varphi'\rightarrow\theta,\varphi)$ measures the proportion of L_s that is reflected on the sea surface when traveling from the direction (θ',φ') to (θ,φ). The quantity $t(\lambda,\ \theta',\varphi'\rightarrow\theta,\varphi)$ represents the radiance transmittance of the sea surface, indicating how much of the L_u in any upward direction (θ',φ') is transmitted through the surface into the upward direction (θ,φ). The hemispheres of all downward and upward directions are denoted as $2\pi_d$ and $2\pi_u$, respectively. Equation (1) can be simplified as

$$L_t(\lambda,\theta,\varphi) = L_r(\lambda,\theta,\varphi) + L_w(\lambda,\theta,\varphi) \tag{2}$$

where L_r refers to the skylight reflected by the surface, as indicated by the first term on the right-hand side of Eq. (1). In order to obtain L_w, L_r must be removed from L_t. As shown in [7], L_r can be estimated according to following equation:

$$L_r(\lambda,\theta,\varphi) = \rho(\lambda,\theta,\varphi)L_s(\lambda,\ \theta'',\varphi) \tag{3}$$

Here θ'' is zenith angle for the measurement of L_s, and ρ is defined as the effective sea-surface reflectance, which is equal to

$$\rho(\lambda,\theta,\varphi) = \frac{\frac{1}{\Omega_{FOV}}\int_{\Omega_{FOV}}\left[\int_{2\pi_d} L_s(\lambda,\ \theta',\varphi')\cdot r(\lambda,\theta',\varphi'\rightarrow\theta,\varphi)d\Omega(\theta',\varphi')\right]d\Omega(\theta,\varphi)}{L_s(\lambda,\ \theta'',\varphi)} \tag{4}$$

or

$$\rho(\lambda,\theta,\varphi) = \frac{L_t(\lambda,\theta,\varphi) - L_w(\lambda,\theta,\varphi)}{L_s(\lambda,\theta'',\varphi)} \tag{5}$$

Thus, a common approach to calculate R_{rs} from AWA measurements can be given by the equation:

$$R_{rs}(\lambda) = \frac{L_t(\lambda,\theta,\varphi)\ -\rho(\lambda,\ \theta,\varphi)\,L_s(\lambda,\ \theta'',\varphi)}{E_s(\lambda)} \tag{6}$$

From this equation, L_t, L_s, and E_s are obtained directly from the radiometer sensors and the key variable to estimate R_{rs} using the AWA approach is ρ. The variability of ρ is dependent on the sky radiance distribution, wavelength, surface conditions (wind speed and wave height), sun zenith angle and viewing geometry. For a flat sea surface and an overcast sky, ρ is usually approximate to the Fresnel reflectance of the sea surface averaged over the FOV of the radiometer. When the sea surface is rough and the skylight is non-uniform, however, ρ changes spectrally since the sea surface effectively integrates over a larger area of the sky than that defined by the sensor's FOV over a flat sea surface. In earlier studies, Mobley [7] provided a look-up table (LUT) of ρ for various sun angles, wind speeds and viewing directions. A spectrally constant ρ (0.028) was recommended for a viewing direction of 40° from the nadir and 135° from the sun. The look-up table of Mobley [7] is based on radiative transfer simulations from the skylight model of Harrison and Coombes [8], in which the radiance of the skylight is scaled empirically from the sky total

Optics EXPRESS

diffuse irradiance. The scaling parameter is spectrally flat for any given direction, which results in the same spectral characteristics for skylight from all directions. This is not consistent with observations and measurements of the sky [9,10]. With the application of a spectrally constant ρ, different levels of uncertainties will be introduced to R_{rs} estimated from Eq. (6).

Over the past few decades, various revisions of Eq. (6) have been proposed to remove sky glint and/or sun glint [11–15]. The differences between these revisions are associated primarily with how sky glint (or sun glint) is removed from the surface signal. Among these approaches, the most widely used assumes that the near-infrared (NIR) water-leaving signal is zero, and thus L_t signal in the NIR is entirely due to glint [1]. For optically complex waters, this assumption is not valid as the NIR signal is often not zero, and many other methods have been proposed to correct for sky glint (or sun glint) in these waters [13,15,16]. Gould et al. [16], for example, used simultaneous in situ inherent optical properties to derive the glint component at 735 nm. In addition, several other correction schemes use a spectral optimization approach (SOA) [12,14,17]. For example, Lee et al. [14] proposed an SOA to determine the bias of L_w and then used it to eliminate surface-reflected light from the total remote sensing reflectance (T_{rs}, the ratio of L_t to E_s). All of these methods attempt to make surface measurements free from the effects of glint; however, most of them used a spectrally-constant ρ which has been questioned in recent studies [14,18,19].

The main objectives of this study are to assess the spectral dependence of ρ and develop a new model to represent its variation with wavelength. The proposed model is then incorporated into the SOA of Lee et al. [14] to process R_{rs} from AWA. Field measurements collected over a wide range of environmental conditions (including water types, sky conditions, wind speeds, sun glints and viewing geometries) are then used to evaluate the performance of the revised SOA (RSOA). Further evaluation of RSOA is conducted using measurements made by the skylight-blocked approach (SBA). Finally, a field experiment was conducted in order to understand the impact of viewing geometry on the determination of R_{rs} with RSOA.

2. Materials and measurements

2.1. Radiative transfer simulations of sky radiance

Based on the revised version of HydroLight (HL, version 5.1.2) in Lin et al. [20], a series of radiative transfer simulations were carried out to further refine and characterize the model for the parameter ρ. In order to account for the significant impact of sea surface waves on ρ, HL utilized Cox-Munk slope statistics to simulate the surface waves, which take into account both gravity and capillary wave slope effects [21,22]. Additionally, instead of the default Harrison and Coombes [8] in HL, we used SBDART (Santa Barbara DISORT Atmospheric Radiative Transfer) [23,24] to simulate the skylight. Previous studies showed that SBDART can model the radiance distribution of skylight or irradiance accurately [25,26]. In this HydroLight-SBDART (HL_S) coupled model, a standard atmospheric profile (mid-latitude summer) was used to model the atmospheric conditions. A total of three different aerosols (urban, oceanic, and tropospheric) were employed to generate simulations. The aerosol optical depth at 550 nm, $\tau_a(550)$, was set to three different values (0.05, 0.1, 0.15) along with three sun angles ($\theta_s = 0°$, 30°, and 60°), and the model was parameterized for several wind speeds ($w_s = 0$, 1, 5, 10, and 15 m/s). A range of viewing angles were included with four viewing zenith angles ($\theta_v = 0°$, 30°, 45°, and 60°) and four viewing azimuth angles ($\varphi_v = 45°$, 90°, 135°, 180°). Further details of the settings used in the HL_S model can be found in Lin et al. [20].

2.2. AWA measurements

A spectroradiometer (Spectral Evolution SR-1901) was used to measure E_s, L_t and L_s over a spectral range from ~ 280 to 1900nm with a spectral resolution of ~ 1.5 nm. Each measurement

Optics EXPRESS

consisted of 5 scans, and then averaged to give one spectrum. The orientation of the L_t sensor was 40° from nadir and 135° from the solar plane. L_s was measured in the same plane as L_t, but at 40° from zenith.

Measurements were taken from four field campaigns (Fig. 1). The first was the VIIRS Ocean Color Calibration and Validation campaign on the NOAA ship *Nancy Foster* from 2nd to 13th December 2015 (VIIRS2015). Field measurements were collected at 18 stations along the Southeast US Coast and in offshore waters of the Western Atlantic. The measurements represent a range of environmental conditions in different water types (oceanic and turbid waters), sky conditions (clear and overcast sky), wind speeds and sun glint. Further details are given in Table 1. The second and third campaigns were performed in Massachusetts Bay (MassBay) over two days (17th & 18th September 2015) during clear sky conditions when 12 stations were occupied. To study the effects of viewing geometry on R_{rs}, further measurements were carried out in a field campaign on 12th May 2016 in the harbor of the University of Massachusetts at Boston (UMB) during blue sky conditions.

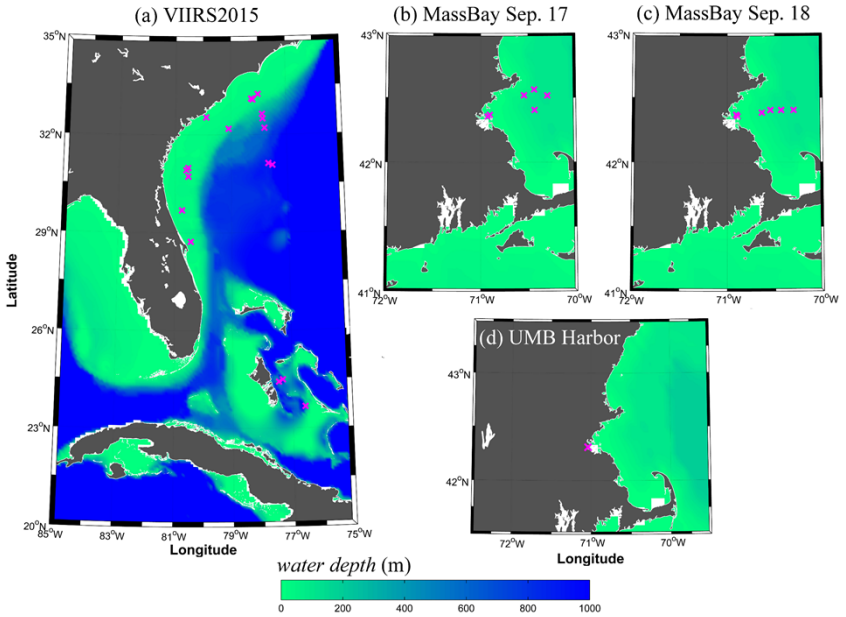

Fig. 1. Maps of measurement locations during four field campaigns: (a) VIIRS cruise in 2015 (VIIRS2015); (b) Massachusetts Bay (MassBay) campaign on 17th September 2015; (c) MassBay campaign on 18th September 2015; and (d) field experiment on 12th May 2016 in the harbor of the University of Massachusetts at Boston (UMB).

2.3. SBA measurements

An SBA was included in the radiometer measurement system to obtain "true" L_w during the field campaigns. This is a robust and accurate method for measuring L_w directly, with the surface-reflected light (sun and sky glint) blocked with a cone attached to the L_w sensor [2]. To avoid any shadowing or reflection effects on the measurements, the system was deployed well away from the research vessel [2]. For each station, the SBA and spectroradiometer were operated almost simultaneously. SBA measurements were recorded for more than 5 minutes, and an averaged L_w was obtained from all L_w spectra after data quality control to ensure that the package inclination was < 5°. More details of the measurement protocol can be found in Lee et al. [2].

Optics EXPRESS

Table 1. Details of stations in VIIRS2015 dataset.

Station	Date in 2015	Julian Day	Time (UTC)	Latitude (°)	Longitude (°)	Sun Zenith (°)	Cloud Cover (%)	Wind Speed (m/s)	Sea State (m)	Water Depth (m)
1	2-Dec	336	19:23	32.54	-79.90	60	65	5.1	0.5	13
2	3-Dec	337	15:00	29.70	-80.74	60	25	5.1	1	33
3	5-Dec	339	14:03	24.42	-77.45	60	20	3.1	0.3	1750
4	5-Dec	339	17:35	24.49	-77.32	45	50	3.1	0.3	1468
5	6-Dec	340	17:48	23.66	-76.58	45	70	5.1	0.3	1500
6	8-Dec	342	18:55	28.73	-80.44	55	40	5.1	0.6	35
7	9-Dec	343	13:55	30.72	-80.54	70	10	5.1	0.6	40
8	9-Dec	343	17:00	30.92	-80.60	50	25	5.1	0.6	40
9	9-Dec	343	19:18	30.99	-80.54	60	40	4.1	0.6	31
10	10-Dec	344	13:00	31.12	-77.67	75	–	–	–	–
11	10-Dec	344	19:06	31.07	-77.53	60	40	3.5	0.6	1000
12	11-Dec	345	13:00	32.20	-77.80	80	50	4.1	0.6	–
13	11-Dec	345	16:06	32.49	-77.88	55	0	4.3	0.6	1000
14	11-Dec	345	18:39	32.63	-77.88	60	0	3.7	0.6	1000
15	12-Dec	346	13:21	33.10	-78.26	75	0	3.6	0.6	50
16	12-Dec	346	16:41	33.24	-78.02	55	0	4.7	0.6	40
17	12-Dec	346	19:36	33.07	-78.21	65	30	2.6	0.6	–
18	13-Dec	347	17:40	32.18	-79.08	55	60	9.1	1	110

3. Method development

3.1. Comparison of sky radiance from HL_S and default HL

Before assessing the spectral dependency of ρ, it is pertinent to compare the sky radiance simulated from HL_S and default HL. The radiative simulations from SBDART of normalized sky radiance (scaled by radiance at 410 nm) for selected solar zenith and viewing geometry angles are shown in Fig. 2(a), (c). The radiance spectra differ significantly at different solar zenith and viewing angles. By comparison, a set of sky radiance spectra using the same geometry angles was also simulated using the default Harrison and Coombes [8] skylight model in Hydrolight. The model was run with a scaling factor (π) derived from the total diffuse irradiance modeled from Gregg and Carder [27]. Figure 2(b), (d) shows the normalized spectrum of sky radiance from the model of Harrison and Coombes [8]. A uniform spectral shape of sky radiance is observed for different solar zenith angles and viewing geometry. This was not consistent with the output from SBDART and the observations of sky radiance [9,10]. Note that for the AWA correction approaches to determine R_{rs} [7,12,17], the radiative simulations of sky radiance were also based on the models of Gregg and Carder [27] and Harrison and Coombes [8], thus further improvement of these approaches to accurately derive R_{rs} is still required.

3.2. Modelling of spectral ρ

With the above radiative simulations using HL_S, ρ is calculated using Eq. (5). For the sky radiance data shown in Fig. 2, the resulting ρ spectra for various sun zenith and viewing angles are shown in Fig. 3. The distribution of ρ from SBDART increases at longer wavelengths (Fig. 3(a), (c)), which is consistent with the previous findings on the wavelength dependency of ρ [14,19]. By comparison, ρ spectra derived from the model of Harrison and Coombes [8] are mostly flat (Fig. 3(b), (d)).

Optics EXPRESS

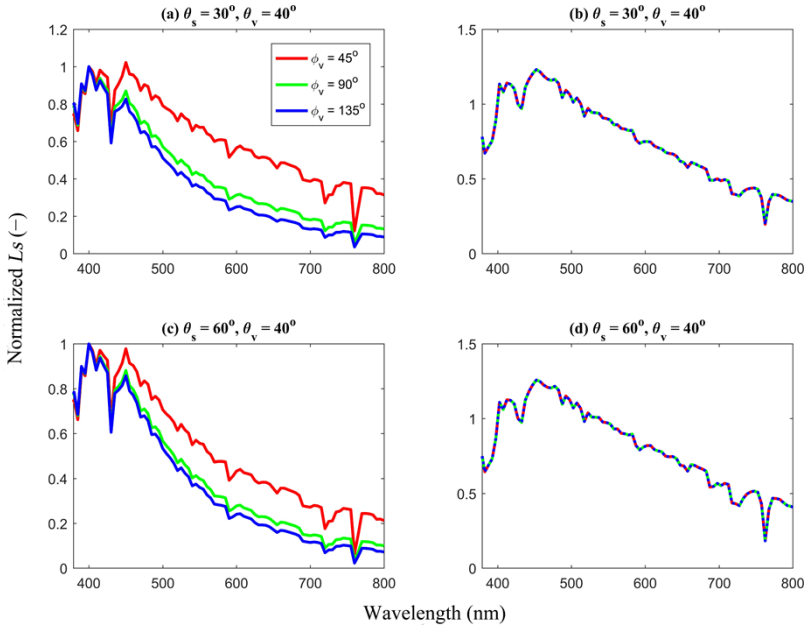

Fig. 2. Normalized sky radiance spectra (scaled by radiance at 410 nm) at different solar zenith and viewing angles. (a), (c) sky radiance simulated by SBDART; (b), (d) sky radiance simulated by the model of Harrison and Coombes [8].

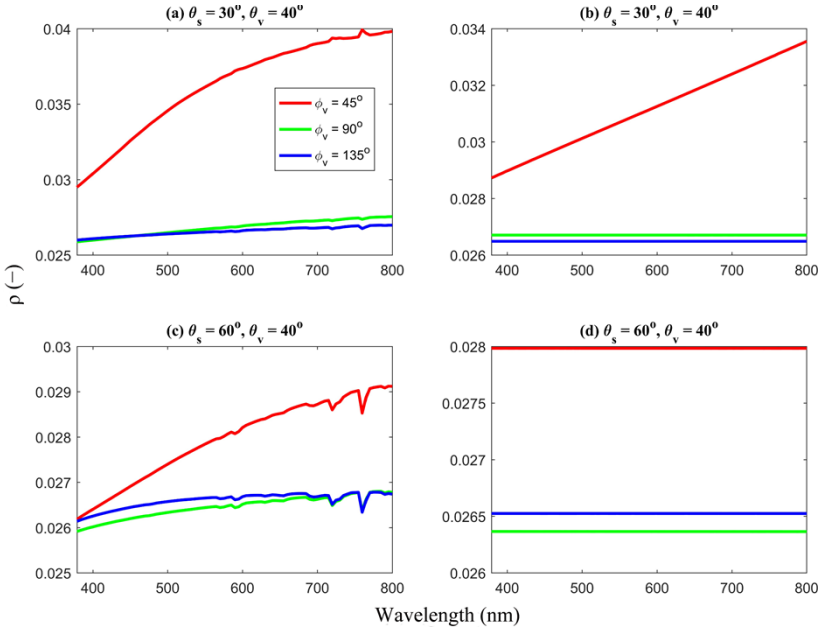

Fig. 3. Distributions of ρ spectra with sky radiance from Fig. 2 calculated using Eq. (5).

Optics EXPRESS

We also investigated the distribution of ρ spectra from SBDART over a range of wind speeds from 0 to 15 m/s (Fig. 4). The magnitude of ρ over the entire spectrum increases significantly with increasing wind speed, as higher wind speeds could result in more sun glint being observed. In addition to wind speed, the aerosol also has an impact on the spectral feature of ρ. To illustrate this impact, Fig. 5 displays the distribution of ρ spectra obtained from SBDART simulations for different values of $\tau_a(550)$ and aerosol types (urban, oceanic, and tropospheric). The ρ spectra exhibit variations with respect to both the aerosol optical depths (Fig. 5(a), (c)) and types (Fig. 5(b), (d)). Despite the differences in the values, the shape of the ρ spectra remains relatively consistent.

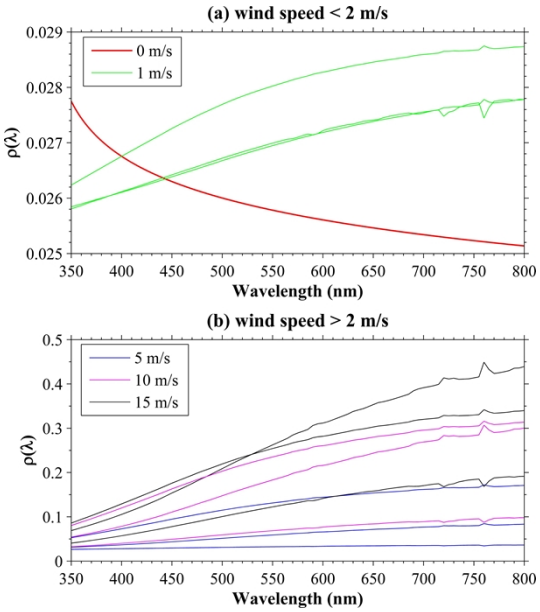

Fig. 4. Distribution of ρ(λ) for various wind speeds with the ρ values calculated from radiative simulations with the Hydrolight-SBDART model.

The spectra of ρ presented in the figures above exhibit similar shapes, and our analysis revealed that these spectra can be effectively described by a power-law function:

$$\rho(\lambda) = h_0 \cdot \left(\frac{\lambda}{550}\right)^{h_1} \tag{7}$$

where h_0 and h_1 are model parameters that vary for different ρ spectra. This formula contrasts with previous skylight correction algorithms [12,17], which assume ρ to be spectrally constant. Fig. 6 shows a comparison of HL_S simulated ρ and those modeled using Eq. (7). The power-law function can model ρ accurately with a small mean absolute percentage deviation (MAPD) (~1.5%) compared to ρ derived using Eq. (7), where MAPD is defined as:

$$MAPD = \frac{1}{n}\sum_{i=1}^{n}\left|\frac{\rho_m - \rho_{HL\_S}}{\rho_{HL\_S}}\right| \tag{8}$$

with ρ_{HL_S} and ρ_m representing ρ from HL_S and that from Eq. (7), respectively.

3.3. RSOA to remove surface-reflected light

The original SOA by Lee et al. [14] used a spectrally constant ρ to eliminate the surface contribution of skylight in producing R_{rs}. In this study, we extend the SOA by incorporating the

Optics EXPRESS

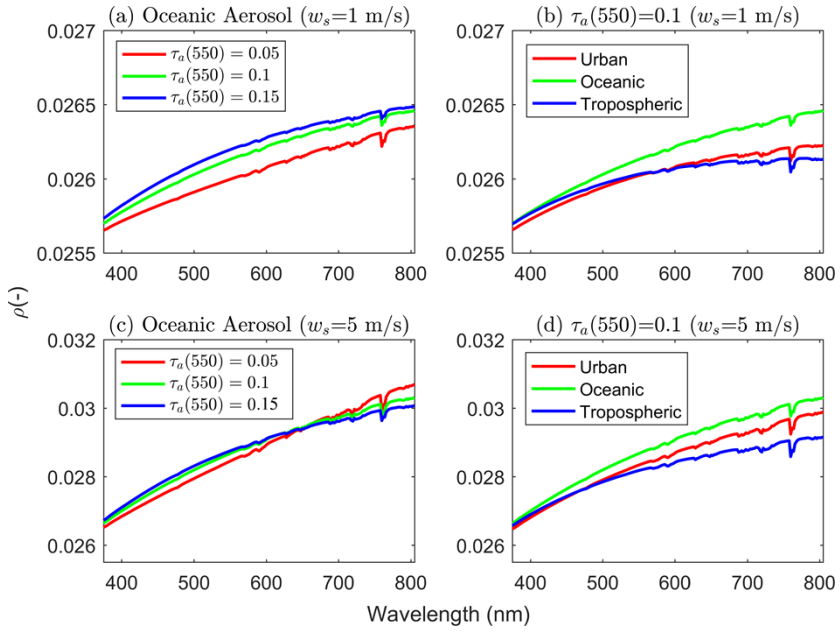

Fig. 5. Examples illustrating the influence of aerosol optical depths (Fig. 5(a) and (c)) and types (Fig. 5(b) and (d)) on the ρ spectra.

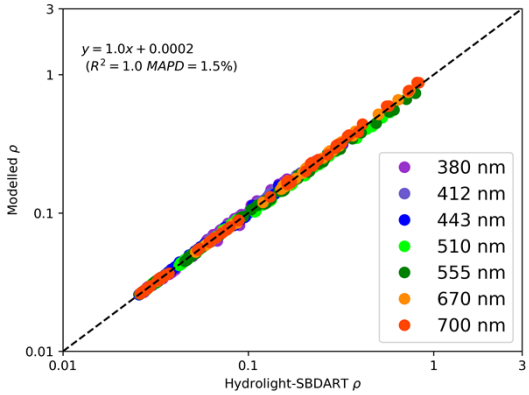

Fig. 6. Comparison of Hydrolight-SBDART ρ with those calculated using Eq. (7).

spectral model of ρ (Eq. (7)). The revised SOA has a similar parameter setup to the original one, but a genetic algorithm (GA) is used instead [28]. More details of the RSOA can be found in the Appendix.

4. Results and discussions

4.1. Comparison of different correction approaches with field measurements

To highlight the new algorithm's performance, we compared four approaches for calculating R_{rs} from AWA measurements. These included the conventional method of Mobley [7] (M99), the 3C method [12,17], the original SOA of Lee et al. [14] (SOA2010), and the RSOA in this study.

Optics EXPRESS

In M99, R_{rs} was derived following:

$$R_{rs}(\lambda) = \frac{L_t(\lambda) - \rho \cdot L_s(\lambda)}{E_s(\lambda)} - \Delta R_{rs} \tag{9}$$

where a spectrally constant ρ was taken from the look-up table in Mobley [29] according to the viewing geometry and wind speed, and ΔR_{rs} was included by setting $R_{rs}(850)$ as 0. In the 3C method, R_{rs} was calculated using Python code developed by the authors. In addition, an optimized ρ from SOA2010 was adopted instead of using a pre-selected constant of Fresnel reflectance.

4.1.1. VIIRS2015 dataset

Firstly, the correction approaches were evaluated using the VIIRS2015 dataset. The field measurements were collected at 18 stations covering various water types (blue open ocean, brown and green coastal water) with $R_{rs}(490)$ varying from ~ 0.0002 to 0.007 sr^{-1} and under different environmental conditions (e.g., clear sky, haze or scattered clouds, varying waves at the sea surface). A list of these measurements can be found in Table 1. To highlight the optimal performance of the RSOA in this study, the clear sky measurements were firstly selected (9 stations with cloud coverage ≤ 30%).

Figure 7 compares the SBA-measured R_{rs} ($R_{rs}{}^{SBA}$) with those derived from AWA approaches. Different performance was observed for the four approaches in correcting the above-water measurements. Generally, M99 overestimated R_{rs}, especially at short wavelengths (< 550 nm, Fig. 7 blue lines). The SOA2010 and 3C methods improved the estimation of R_{rs} over the whole spectrum. The RSOA method exhibited the most accurate glint correction using a wavelength dependent ρ. More details also can be found in Table 2.

Table 2. Statistics for mean absolute percentage deviation (MAPD)[a] and mean absolute deviation (MAD)[b] in the comparison of $R_{rs}{}^{SBA}$ with those from different correction approaches for the VIIRS2015 dataset.

Station	MAPD (%)				MAD (sr^{-1})			
	RSOA	M99	SOA2010	3C	RSOA	M99	SOA2010	3C
2	**9.8**	***82.2***	***64.9***	***38.1***	**1.3E-04**	**7.2E-04**	**4.7E-04**	**7.0E-04**
3	63.9	49.5	38.3	39.2	1.8E-04	6.3E-04	4.9E-04	3.3E-04
7	17.1	37.7	25.1	23.8	3.3E-04	5.5E-04	4.5E-04	5.7E-04
8	**13.2**	**115.6**	**46.7**	**84.4**	**3.7E-04**	**2.9E-03**	**1.2E-03**	**1.9E-03**
13	**10.5**	**46.1**	**16.1**	**27.4**	**1.2E-04**	**8.2E-04**	**3.8E-04**	**4.6E-04**
14	23.9	57.7	29.4	51.1	3.6E-04	3.3E-04	1.3E-04	6.1E-04
15	**9.0**	**37.8**	**11.7**	**24.3**	**2.1E-04**	**1.6E-03**	**4.8E-04**	**6.4E-04**
16	18.2	22.9	26.5	23.2	1.3E-04	4.5E-04	3.2E-04	4.2E-04
17	39.1	74.1	73.2	61.8	3.5E-04	9.9E-04	9.1E-04	9.7E-04

[a] $MAPD = \frac{1}{n}\sum_{i=1}^{n}\left|\frac{R_{rs}(\lambda_i)^C - R_{rs}(\lambda_i)^{SBA}}{R_{rs}(\lambda_i)^{SBA}}\right|$

[b] $MAD = \frac{1}{n}\sum_{i=1}^{n}|R_{rs}(\lambda_i)^C - R_{rs}(\lambda_i)^{SBA}|$ where $R_{rs}(\lambda_i)^C$ are corrected R_{rs} with different correction approaches and $R_{rs}(\lambda_i)^{SBA}$ are SBA-measured R_{rs}; the best performance of RSOA is highlighted in bold.

The performance of RSOA was not affected by water type. For coastal waters (e.g., Fig. 7(c) and Fig. 7(g), (h)), R_{rs} estimated from RSOA were in good agreement with $R_{rs}{}^{SBA}$ and this consistency was also observed for turbid brown water (Fig. 7(h)), where both the spectral shape and magnitude were very similar. For blue waters, although some L_t measurements (Fig. 7(a),

Optics EXPRESS

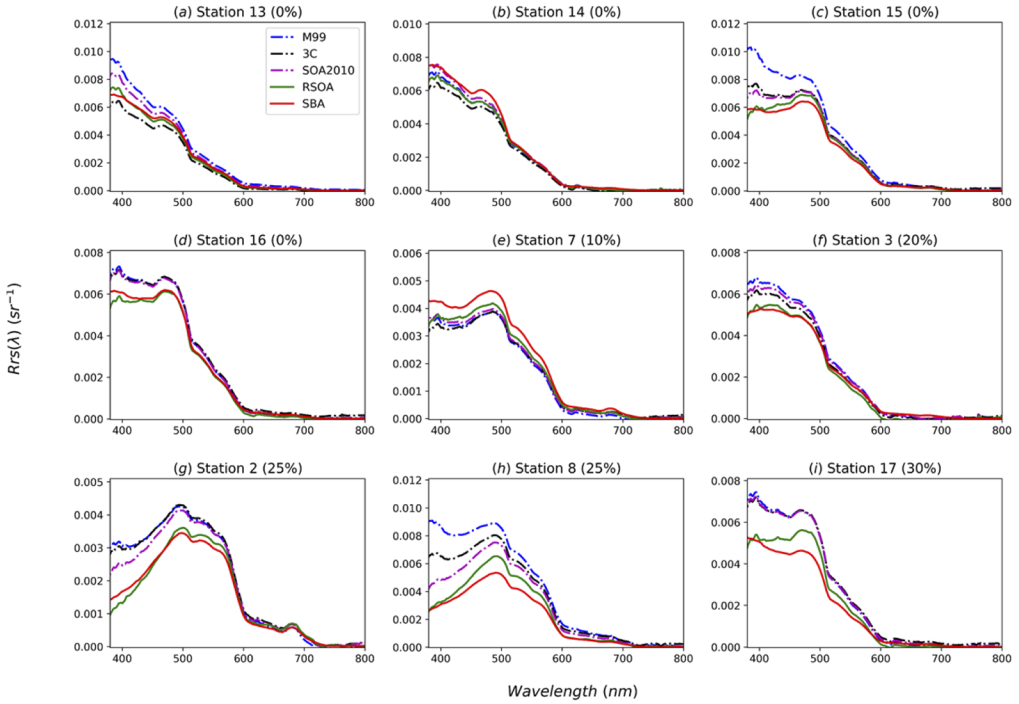

Fig. 7. A comparison of $R_{rs}{}^{SBA}$ with those from four different correction approaches with clear sky measurements (cloud coverage ≤ 30%) in the VIIRS2015 dataset. The correction approaches include the most conventional method of Mobley [7] (M99), the 3C method [12,17], the SOA of Lee et al. [14] (SOA2010), and the revised SOA (RSOA).

(b)) were affected by sun glint, RSOA still performed very well in removing sun glint from L_t. These results illustrate that RSOA can be applied with confidence and accuracy in a wide range of water types.

Fig. 8 shows scatter plots of the different approaches against the $R_{rs}{}^{SBA}$. M99-estimated R_{rs} generally agrees well with the SBA measurements ($R^2 = 0.81$, and MAPD = 58.2%), but it generally overestimates R_{rs} over the entire spectrum. The 3C approach shows large deviations from the SBA measurements due to overcorrection of the spectra (MAPD = 41.5%), which could be attributed to the incorrect ρ in the 3C approach, and leads to an overcorrection of surface-reflected radiance from L_t. High scatter at 380 and 442 nm was observed in both M99 and 3C approaches due to the influence of sun glint. The SOA2010 approach improved on both M99 and 3C ($R^2 = 0.94$, MAPD = 36.9%). The RSOA approach exhibited the highest accuracy with $R^2 = 0.97$ and MAPD = 22.3% (Fig. 8(d)), which decreased to ~ 11% for $R_{rs} > 0.0005$ sr^{-1}. These results emphasize the superior performance of RSOA in correcting sun glint in above water measurements.

Sky conditions can have a significant impact on estimates of R_{rs} using AWA measurements [6,30]. To assess the performance of correction approaches under partially cloudy or cloudy conditions, we analyzed their performance in these conditions, as shown in Fig. S1 (see Supplement 1). The 3C approach proved to be better than M99, though in some specific cases, 3C resulted in incorrect values (e.g., negative R_{rs} values at station 1). Using SOA2010, most of the derived R_{rs} were more accurate than M99 and 3C spectra. RSOA derived R_{rs} showed the best agreement with $R_{rs}{}^{SBA}$ (Fig. S2).

Optics EXPRESS

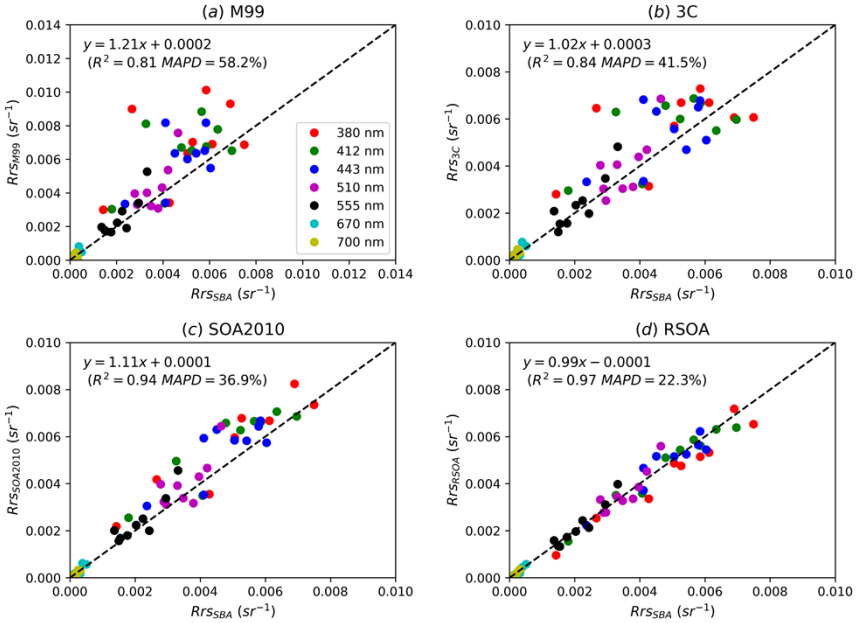

Fig. 8. Comparison between R_{rs}^{SBA} and those derived by (a) M99, (b) 3C, (c) SOA2010, and (d) RSOA in this study.

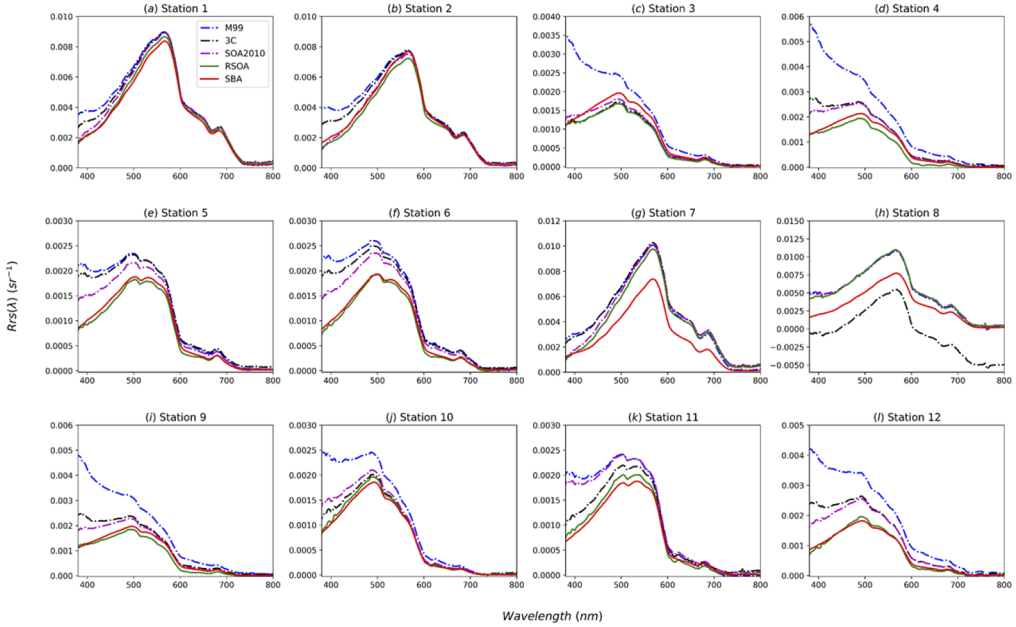

Fig. 9. As Fig. 7 but for the measurements collected in Massachusetts Bay.

4.1.2. Massachusetts Bay dataset

The MassBay measurements were primarily taken in green and brown waters with Secchi depths ranging from ~3−12 m. The measurements were collected mainly under clear blue skies. In

Optics EXPRESS

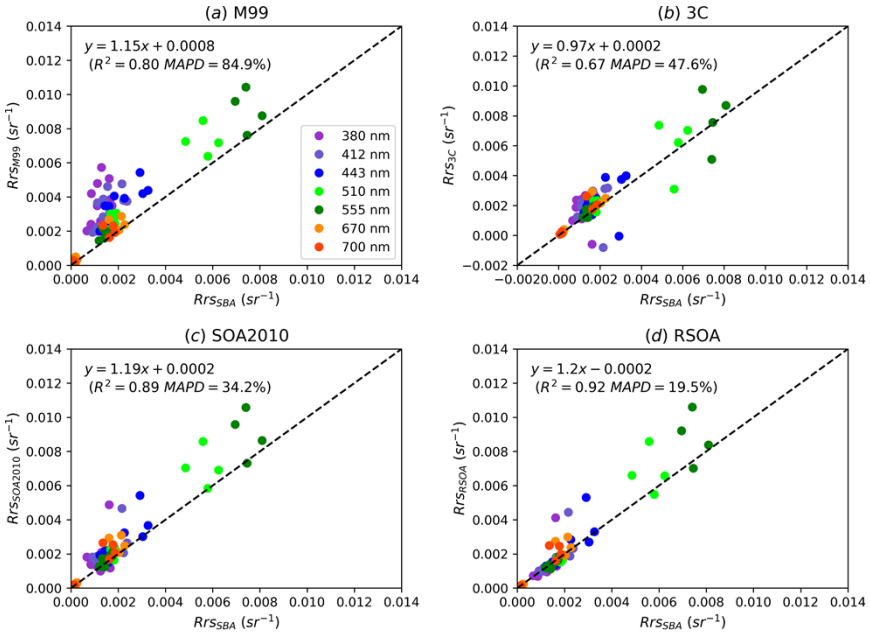

Fig. 10. As Fig. 8 but for the data of MassBay.

Table 3. As Table 2 but for MassBay dataset.

Station	MAPD (%)				MAD (sr^{-1})			
	RSOA	M99	SOA2010	3C	RSOA	M99	SOA2010	3C
1	**4.2**	***32.2***	***9.9***	***21.6***	**1.5E-04**	**8.6E-04**	**3.3E-04**	**6.1E-04**
2	**7.3**	**36.5**	**6.8**	**22.7**	**2.7E-04**	**8.1E-04**	**1.4E-04**	**5.1E-04**
3	19.9	70.1	10.9	13.2	1.6E-04	7.8E-04	1.0E-04	1.3E-04
4	29.8	150.1	25.4	40.3	1.5E-04	1.7E-03	3.4E-04	4.8E-04
5	**7.4**	**56.3**	**29.7**	**55.7**	**6.5E-05**	**5.1E-04**	**2.6E-04**	**4.6E-04**
6	**6.3**	**72.8**	**37.6**	**60.1**	**5.4E-05**	**6.4E-04**	**3.3E-04**	**5.1E-04**
7	39.8	71.4	50.5	72.1	1.3E-03	1.6E-03	1.3E-03	1.7E-03
8	62.0	82.8	84.2	132.8	2.2E-03	2.2E-03	2.3E-03	3.1E-03
9	22.4	133.9	21.3	42.9	1.3E-04	1.4E-03	2.7E-04	4.5E-04
10	**5.0**	**72.4**	**26.1**	**15.6**	**3.2E-05**	**6.2E-04**	**2.1E-04**	**1.1E-04**
11	**12.6**	**66.2**	**61.3**	**26.2**	**8.0E-05**	**5.8E-04**	**5.2E-04**	**2.3E-04**
12	11.8	174.1	48.7	70.2	6.2E-05	1.5E-03	4.8E-04	6.8E-04

these types of waters, the R_{rs} at NIR are generally larger than 0, thus setting R_{rs} to zero at this wavelength could be questionable.

To evaluate the performance of different correction approaches, Fig. 9 shows a comparison of $R_{rs}{}^{SBA}$ with those corrected by four different approaches. The RSOA approach proved to be more reliable and accurate than the other three methods in estimating R_{rs}. Even under conditions where the other models showed high sun glint contamination, the RSOA approach still obtained very reasonable R_{rs} values, as demonstrated by stations 3, 4, and 12 in Fig. 9.

The scatter plots further supported the superior performance of the RSOA approach ($R^2 = 0.92$, and MAPD = 19.5%) compared to the other approaches, as shown in Fig. 10. Full details of

Optics EXPRESS

the statistical metrics for each approach and station are provided in Table 3. These results provide strong evidence of the effectiveness and robustness of the RSOA approach, even under challenging conditions, and highlight its potential to improve the accuracy and reliability of remote sensing reflectance measurements in green and brown waters.

4.2. Dependency on viewing geometry

Removing surface-reflected light for above-water measurements is highly challenging because of the ambiguous and unpredictable glints due to surface waves [6,7,30–32]. Mobley [7] recommended an optimal measurement geometry to minimize the effect of glint. Generally, a viewing geometry of 40° from the nadir (θ_v) and 135° from the sun (φ_v) was suggested for the measurement of L_t, and a θ_v of 40° from zenith and φ_v of 135° from azimuth is required for the measurement of L_s [7]. In the field, achieving this is highly dependent on the salient sea conditions and especially on the wave conditions, where the viewing geometry of radiometers relative to the position of the sun is not stable. In particular, for a continuous underway system [30], φ_v often varies over a wide range (e.g., ~50°−160°), which could differ significantly from the recommended optimal φ_v (135°).

The above-water measurements taken in the UMB harbor were used to further understand the impact of viewing geometry on the determination of $R_{rs}(\lambda)$. The measurements were collected under blue skies with a solar zenith angle of ~ 30°. Several viewing geometries were used to measure L_s and L_t ($\varphi_v = 45°$, 90°, 135°, and 180°, and $\theta_v = 30°$, 45°, and 60°). For each viewing geometry (φ_v, θ_v), a total of 5 attempts were performed to obtain concurrent measurements of E_s, L_s, and L_t. A total of 60 R_{rs} spectra were estimated for each correction approach.

Fig. 11 shows the $R_{rs}{}^{SBA}$ compared with those derived from the other four approaches. The value of ρ in M99 was taken from the look-up table in Mobley [29] as a function of the viewing geometry. M99 significantly overestimated R_{rs} compared with the SBA measurements (Fig. 11(a)). For both 3C and SOA2010, the derived R_{rs} spectra showed similar magnitudes and shapes with $R_{rs}{}^{SBA}$, but some deviations were still observed (< ~ 450 nm in Fig. 11(b) and Fig. 11(c)). For the

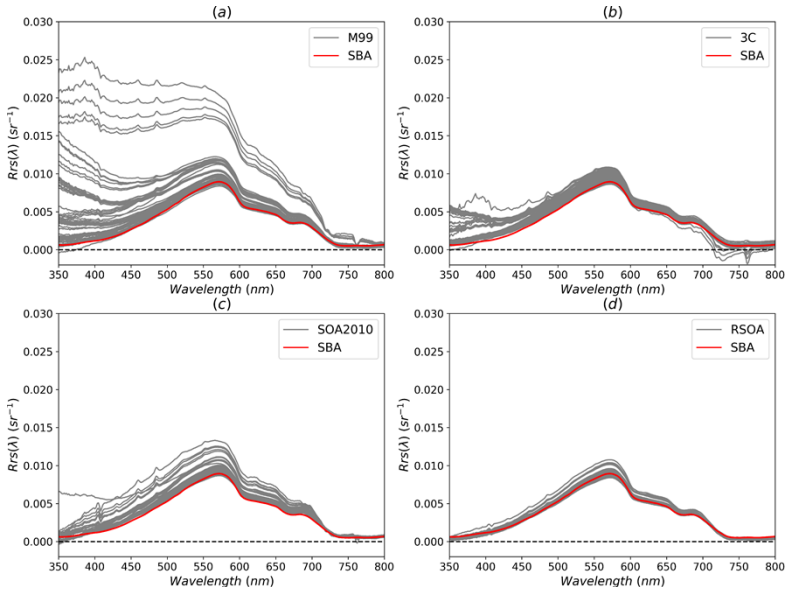

Fig. 11. Dependency of R_{rs} estimations on view geometry for four correction approaches (a) M99, (b) 3C, (c) SOA2010 and (d) RSOA; $R_{rs}{}^{SBA}$ spectra are shown for comparison.

Optics EXPRESS

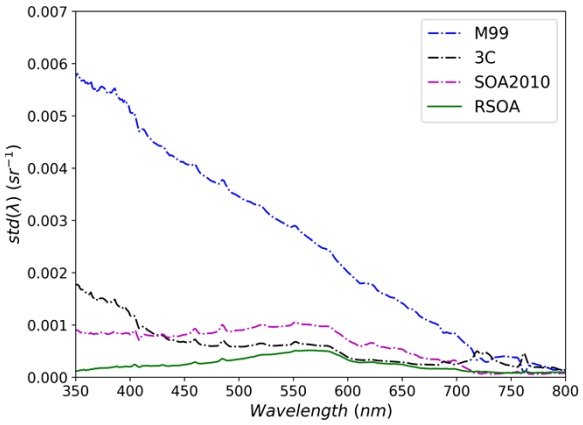

Fig. 12. Standard deviation (STD) of all estimated $R_{rs}(\lambda)$ shown in Fig. 11 from the four correction approaches.

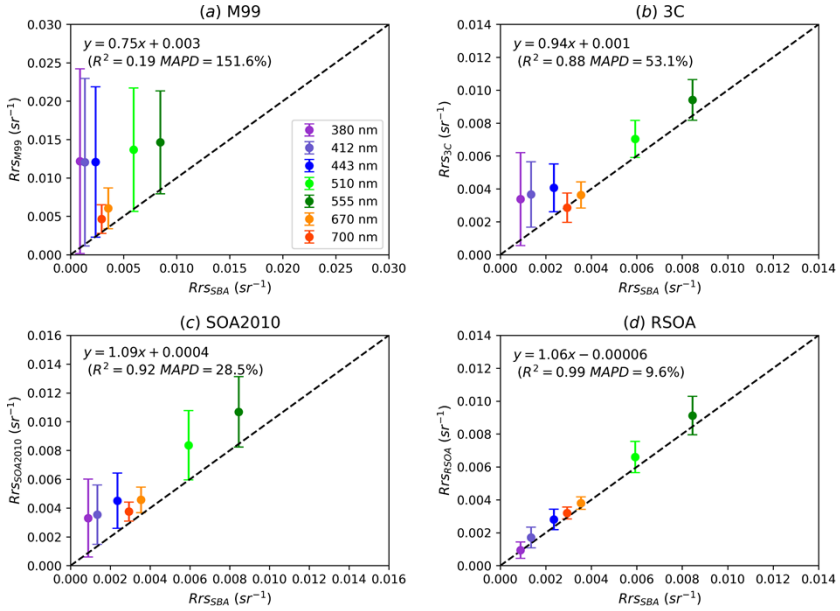

Fig. 13. Scatter plots of R_{rs}^{SBA} with those estimated from different approaches in the experiment conducted at the harbor of UMB, where the dot refers to the median value and the error bar indicates the range of the estimated R_{rs} in each wavelength.

RSOA, the estimated R_{rs} spectra were more consistent with the R_{rs}^{SBA} (Fig. 11(d)). Fig. 12 shows the standard deviation (STD) of the different approaches to estimating R_{rs}. R_{rs} estimated with RSOA had the lowest STD among all the approaches tested, illustrating a superior performance of this model and approach. When the methods were compared as scatter plots, they clearly indicated that the sensitivity of RSOA to the viewing geometry is at a minimum at each wavelength. Overall there is a better agreement between RSOA estimates and measurements from SBA (Fig. 13).

Optics EXPRESS

5. Summary

Through both radiative simulations and field measurements, we observe that ρ is spectrally dependent and this spectral dependence can be empirically modeled as a power-law function of wavelength. With this wavelength-dependent ρ model, the previous SOA2010 processing scheme was further extended using the RSOA approach. This new scheme was evaluated against three other methods (M99, 3C, and SOA2010) using independent field measurements collected during four campaigns covering different environmental conditions. Our results showed that the RSOA approach obtained more reliable and accurate *Rrs* compared to the other three schemes, and was effective in removing sun glint contamination, which has been a major challenge for AWA measurements. Furthermore, this approach also exhibited a relatively low dependency on measurement viewing geometry. The RSOA approach holds great potential for improving ocean-color data required for developing remote sensing algorithms and validating satellite products.

Appendix

With the new $\rho(\lambda)$ model (Eq. (7)), total remote-sensing reflectance (T_{rs}, ratio of L_T to E_s) is expressed in the following equation:

$$T_{rs}(\lambda) = R_{rs}(\lambda) + \left[h_0 \cdot \left(\frac{\lambda}{550}\right)^{h_1}\right] \cdot S_{rs}(\lambda) + \Delta R_{rs} \tag{A1}$$

where S_{rs} is the skylight reflectance (the ratio of L_s to E_s), and ΔR_{rs} is a spectrally-flat residual term representing radiative contributions due to foam, sea spray and whitecaps. For comparison the derivation of $R_{rs}(\lambda)$ from Lee et al. [14] is given as:

$$R_{rs}(\lambda) \approx f[a(\lambda), b_b(\lambda)] \tag{A2}$$

where $a(\lambda)$ and $b_b(\lambda)$ are the absorption and backscattering coefficients, respectively, and their values are based on the additive contribution of the optically active in water components (seawater (w), phytoplankton (ph), detritus (d), and gelbstoff (g)) [33,34].

$$a(\lambda) = a_w(\lambda) + a_{ph}(\lambda) + a_{dg}(\lambda) \tag{A3}$$

$$b_b(\lambda) = b_{bw}(\lambda) + b_{bp}(\lambda) \tag{A4}$$

where the subscript "p" in Eq. (A4 denotes particles, including phytoplankton and detritus. Literature values of $a_w(\lambda)$ [35,36] and $b_{bw}(\lambda)$ [37] are used. As in Lee et al. [38], $a_{ph}(\lambda)$ is expressed as a nonlinear function of $a_{ph}(440)$

$$a_{ph}(\lambda) = [a_0(\lambda) + a_1(\lambda) \cdot ln(a_{ph}(440))] \cdot a_{ph}(440) \tag{A5}$$

The spectral dependency of $a_{dg}(\lambda)$ is modeled using an exponential function [39]

$$a_{dg}(\lambda) = a_{dg}(440) \cdot exp[-S_{dg}(\lambda - 440)] \tag{A6}$$

where S_{dg} is the slope of the exponential model which is assumed to be constant ($0.015\ \mathrm{nm}^{-1}$) for this study. The spectral dependency of $b_{bp}(\lambda)$ is modeled following as follows [40,41]:

$$b_{bp}(\lambda) = b_{bp}(400) \cdot \left(\frac{\lambda}{400}\right)^{-\eta} \tag{A7}$$

where η is calculated from initial $R_{rs}(\lambda)$ ($R_{rs}{}^{\mathrm{In}}(\lambda)$).

$$\eta = 2.2 \cdot \left(1 - 1.2 \cdot e^{-0.9 \cdot \frac{R_{rs}^{In}(440)}{R_{rs}^{In}(555)}}\right) \tag{A8}$$

Optics EXPRESS

$$R_{rs}^{In}(\lambda) = T_{rs}(\lambda) - \rho \cdot S_{rs}(\lambda) - \Delta R_{rs}(750) \tag{A9}$$

and ρ is pre-selected according to the viewing geometry [29]. Using these bio-optical models, $R_{rs}(\lambda)$ can be approximately determined by three unknowns ($a_{ph}(440)$, $a_{dg}(440)$, and $b_{bp}(400)$).

In Eq. A2 there are six unknowns that can be retrieved using the genetic algorithm (GA in MATLAB optimization toolbox [28]) following initial parameterization [38]:

$$[a_{ph}(440)]^{In} = 0.072 \cdot \left(\frac{R_{rs}^{In}(440)}{R_{rs}^{In}(550)}\right)^{-1.62} \tag{A10}$$

$$[a_{dg}(440)]^{In} = [a_{ph}(440)]^{In} \tag{A11}$$

$$[b_{bp}(400)]^{In} = 30 \cdot a_w(640) \cdot R_{rs}^{In}(640) \tag{A12}$$

$$[h_0]^{In} = 0.032 \tag{A13}$$

$$[h_1]^{In} = 0.1 \tag{A14}$$

$$\Delta R_{rs}{}^{In} = \Delta R_{rs}(750) \tag{A15}$$

The boundaries of these unknown variables are set as

$$0.003 < a_{ph}(440) \tag{A16}$$

$$0.001 < a_{dg}(440) \tag{A17}$$

$$0.0001 < b_{bp}(400) \tag{A18}$$

$$h_0 < 0.5 \tag{A19}$$

$$-0.1 < h_1 < 0.5 \tag{A20}$$

$$0 < \Delta R_{rs} < 0.05 \cdot R_{rs}^{In}(490) \tag{A21}$$

To highlight the spectral difference between $R_{rs}(\lambda)$ and $S_{rs}(\lambda)$, the shortest wavelength is extended to 350 nm. Finally, the cost function is defined as:

$$Fun_{cost} = \left(\frac{1}{n}\left[\sum_{\lambda=350}^{600}\left(\frac{T_{rs}(\lambda) - esT_{rs}(\lambda)}{T_{rs}(\lambda)}\right)^2 + \sum_{\lambda=750}^{800}\left(\frac{T_{rs}(\lambda) - esT_{rs}(\lambda)}{T_{rs}(\lambda)}\right)^2\right]\right)^{0.5} \tag{A22}$$

where $T_{rs}(\lambda)$ is the field measurement and $esT_{rs}(\lambda)$ is the estimated $T_{rs}(\lambda)$ via Eq. (A2). To avoid the influence of chlorophyll fluorescence, the wavelength range is set from 350 to 600 nm and 750 to 800 nm.

Funding. European Commission Horizon 2020 project Copernicus Evolution – Research for harmonised and Transitional-water Observation (CERTO, 870349); European Space Agency AMT4OceanSatFlux (4000125730/18/NL/FF/gp), AMT4CO2Flux (4000136286/21/NL/FF/ab); Natural Environment Research Council (NERC) National Capability funding to Plymouth Marine Laboratory for the Atlantic Meridional Transect (CLASSAMT).

Acknowledgments. The authors would like to thank the captain and crew of the NOAA ship Nancy Foster. This work was supported by the Joint Polar Satellite System (JPSS) funding for the NOAA ocean color calibration and validation (Cal/Val) project. Some of the in-situ data used in this study were collected from the NOAA dedicated VIIRS ocean color calibration and validation (Cal/Val) cruises supported by the Joint Polar Satellite System (JPSS) program and the NOAA Office of Marine and Aviation Operations.

Disclosures. The authors declare no conflicts of interest.

Data availability. Data underlying the results presented in this paper are not publicly available at this time but may be obtained from the authors upon reasonable request.

Supplemental document. See Supplement 1 for supporting content.

Optics EXPRESS

References

1. S. B. Hooker, G. Lazin, G. Zibordi, and S. McLean, "An evaluation of above-and in-water methods for determining water-leaving radiances," J. Atmos. Oceanic Technol. **19**(4), 486–515 (2002).
2. Z. Lee, N. Pahlevan, Y.-H. Ahn, S. Greb, and D. O'Donnell, "Robust approach to directly measuring water-leaving radiance in the field," Appl. Opt. **52**(8), 1693–1701 (2013).
3. G. Zibordi, S. Hooker, J. Berthon, and D. D'Alimonte, "Autonomous above-water radiance measurements from an offshore platform: a field assessment experiment," J. Atmos. Oceanic Technol. **19**(5), 808–819 (2002).
4. R. C. Smith, C. R. Booth, and J. L. Star, "Oceanographic biooptical profiling system," Appl. Opt. **23**(16), 2791–2797 (1984).
5. K. G. Ruddick, K. Voss, E. Boss, A. Castagna, R. Frouin, A. Gilerson, M. Hieronymi, B. C. Johnson, J. Kuusk, and Z. Lee, "A review of protocols for fiducial reference measurements of water-leaving radiance for validation of satellite remote-sensing data over water," Remote Sens. Environ. **11**(19), 2198 (2019).
6. G. Zibordi, F. Mélin, J.-F. Berthon, B. Holben, I. Slutsker, D. Giles, D. D'Alimonte, D. Vandemark, H. Feng, and G. Schuster, "AERONET-OC: a network for the validation of ocean color primary products," J. Atmos. Oceanic Technol. **26**(8), 1634–1651 (2009).
7. C. D. Mobley, "Estimation of the remote-sensing reflectance from above-surface measurements," Appl. Opt. **38**(36), 7442–7455 (1999).
8. A. Harrison and C. Coombes, "An opaque cloud cover model of sky short wavelength radiance," Sol. Energy **41**(4), 387–392 (1988).
9. E. J. McCartney, *Optics of the Atmosphere: Scattering by Molecules and Particles* (John Wiley Sons, Inc., 1976), p. 421.
10. A. J. Preetham, P. Shirley, and B. Smits, "A practical analytic model for daylight," in *Proceedings of the 26th annual conference on Computer Graphics and Interactive Techniques* (1999), 91–100.
11. S. Garaba and O. Zielinski, "Methods in reducing surface reflected glint for shipborne above-water remote sensing," J. Eur. Opt. Soc.-Rapid Publ. **8**, 13058 (2013).
12. P. M. Groetsch, P. Gege, S. G. Simis, M. A. Eleveld, and S. W. Peters, "Validation of a spectral correction procedure for sun and sky reflections in above-water reflectance measurements," Opt. Express **25**(16), A742–A761 (2017).
13. T. Kutser, E. Vahtmäe, B. Paavel, and T. Kauer, "Removing glint effects from field radiometry data measured in optically complex coastal and inland waters," Remote Sens. **133**, 85–89 (2013).
14. Z. Lee, Y. H. Ahn, C. Mobley, and R. Arnone, "Removal of surface-reflected light for the measurement of remote-sensing reflectance from an above-surface platform," Opt. Express **18**(25), 26313–26324 (2010).
15. K. G. Ruddick, V. D Cauwer, Y. J. Park, and G. Moore, "Seaborne measurements of near infrared water leaving reflectance: The similarity spectrum for turbid waters," Limnol. Oceanogr. **51**(2), 1167–1179 (2006).
16. R. Gould, R. Arnone, and M. Sydor, "Absorption, scattering, and, remote-sensing reflectance relationships in coastal waters: testing a new inversion algorithm," J. Coastal Res. **1**(11), 328–341 (2001).
17. J. Pitarch, M. Talone, G. Zibordi, and P. Groetsch, "Determination of the remote-sensing reflectance from above-water measurements with "3C model": a further assessment," Opt. Express **28**(11), 15885–15906 (2020).
18. T. W. Cui, Q. J. Song, J.-W. Tang, and J. Zhang, "Spectral variability of sea surface skylight reflectance and its effect on ocean color," Opt. Express **21**(21), 24929–24941 (2013).
19. X. Zhang, S. He, A. Shabani, P.-W. Zhai, and K. Du, "Spectral sea surface reflectance of skylight," Opt. Express **25**(4), A1–A13 (2017).
20. J. Lin, Z. Lee, M. Ondrusek, and K. Du, "Remote sensing of normalized diffuse attenuation coefficient of downwelling irradiance," J. Geophys. Res.: Oceans **121**, 6717–6730 (2016).
21. C. Cox and W. Munk, "The measurement of the roughness of the sea surface from photographs of the sun's glitter," (Air Force, Technical Report, U.S.).
22. C. Cox, "Statistics of the sea surface derived from sun glitter," J. Mar. Res. **13**, 198–227 (1954).
23. P. Ricchiazzi, *Input Documentation for SBDART* (Univ. of California, 2002).
24. P. Ricchiazzi, S. Yang, C. Gautier, and D. Sowle, "SBDART: A research and teaching software tool for plane-parallel radiative transfer in the Earth's atmosphere," Bull. Am. Meteorol. Soc. **79**(10), 2101–2114 (1998).
25. J. C. Barnard and D. Powell, "A comparison between modeled and measured clear-sky radiative shortwave fluxes in Arctic environments, with special emphasis on diffuse radiation," J. Geophys. Res. **107**(D19), 1–10 (2002).
26. M. Obregón, A. Serrano, M. J. Costa, and A. M. Silva, "Validation of libRadtran and SBDART models under different aerosol conditions," in *IOP Conference Series: Earth and Environmental Science*, (IOP Publishing, 2015), 012010.
27. W. W. Gregg and K. L. Carder, "A simple spectral solar irradiance model for cloudless maritime atmospheres," Limnol. Oceanogr. **35**(8), 1657–1675 (1990).
28. D. Goldberg and J. Holland, "Genetic algorithms and machine learning," Mach. Learn. **3**(2/3), 95–99 (1988).
29. C. D. Mobley, "Polarized reflectance and transmittance properties of windblown sea surfaces," Appl. Opt. **54**(15), 4828–4849 (2015).
30. J. Lin, G. Dall'Olmo, G. H. Tilstone, R. J. Brewin, V. Vabson, I. Ansko, H. Evers-King, T. Casal, and C. Donlon, "Derivation of uncertainty budgets for continuous above-water radiometric measurements along an Atlantic Meridional Transect," Opt. Express **30**(25), 45648–45675 (2022).

Optics EXPRESS

31. T. Harmel, A. Gilerson, A. Tonizzo, J. Chowdhary, A. Weidemann, R. Arnone, and S. Ahmed, "Polarization impacts on the water-leaving radiance retrieval from above-water radiometric measurements," Appl. Opt. **51**(35), 8324–8340 (2012).
32. T. Harmel, A. Gilerson, S. Hlaing, A. Weidemann, R. Arnone, and S. Ahmed, "Long Island Sound Coastal Observatory: assessment of above-water radiometric measurement uncertainties using collocated multi and hyper-spectral systems: reply to comment," Appl. Opt. **51**(17), 3893–3899 (2012).
33. M. Babin, D. Stramski, G. M. Ferrari, H. Claustre, A. Bricaud, G. Obolensky, and N. Hoepffner, "Variations in the light absorption coefficients of phytoplankton, nonalgal particles, and dissolved organic matter in coastal waters around Europe," J. Geophys. Res. **108**(C7), 3211 (2003).
34. D. Stramski, E. Boss, D. Bogucki, and K. J. Voss, "The role of seawater constituents in light backscattering in the ocean," Prog. Oceanogr. **61**(1), 27–56 (2004).
35. Z. Lee, J. Wei, K. Voss, M. Lewis, A. Bricaud, and Y. Huot, "Hyperspectral absorption coefficient of "pure" seawater in the range of 350–550 nm inverted from remote sensing reflectance," Appl. Opt. **54**(3), 546–558 (2015).
36. R. M. Pope and E. S. Fry, "Absorption spectrum (380–700 nm) of pure water. II. Integrating cavity measurements," Appl. Opt. **36**(33), 8710–8723 (1997).
37. A. Morel, "Optical properties of pure water and pure sea water," Optical Aspects of Oceanography **1**, 22 (1974).
38. Z. Lee, K. L. Carder, C. D. Mobley, R. G. Steward, and J. S. Patch, "Hyperspectral remote sensing for shallow waters: 2. Deriving bottom depths and water properties by optimization," Appl. Opt. **38**(18), 3831–3843 (1999).
39. K. Oubelkheir, H. Claustre, A. Bricaud, and M. Babin, "Partitioning total spectral absorption in phytoplankton and colored detrital material contributions," Limnol. Oceanogr.: Methods **5**, 384–395 (2007).
40. H. R. Gordon and A. Y. Morel, *Remote Assessment of Ocean Color for Interpretation of Satellite Visible Imagery: A Review* (Springer Science, 1983), Vol. 4.
41. R. C. Smith and K. S. Baker, "Optical properties of the clearest natural waters (200–800 nm)," Appl. Opt. **20**(2), 177–184 (1981).